

Exact treatment of magnetism-driven ferroelectricity in the one-dimensional compass modelWen-Long You,¹ Guang-Hua Liu,² Peter Horsch,³ and Andrzej M. Oleś^{3,4}¹*College of Physics, Optoelectronics and Energy, Soochow University, Suzhou, Jiangsu 215006, People's Republic of China*²*Department of Physics, Tianjin Polytechnic University, Tianjin 300387, People's Republic of China*³*Max-Planck-Institut für Festkörperforschung, Heisenbergstrasse 1, D-70569 Stuttgart, Germany*⁴*Marian Smoluchowski Institute of Physics, Jagellonian University, Reymonta 4, PL-30059 Kraków, Poland*

(Received 15 June 2014; published 19 September 2014)

We consider a class of one-dimensional compass models with antisymmetric Dzyaloshinskii-Moriya exchange interaction in an external magnetic field. Based on the exact solution derived by means of Jordan-Wigner transformation, we study the excitation gap, spin correlations, ground-state degeneracy, and critical properties at phase transitions. The phase diagram at finite electric and magnetic field consists of three phases: ferromagnetic, canted antiferromagnetic, and chiral. Dzyaloshinskii-Moriya interaction induces an electrical polarization in the ground state of the chiral phase, where the nonlocal string order and special features of entanglement spectra arise, while strong chiral correlations emerge at finite temperature in the other phases and are controlled by a gap between the nonchiral ground state and the chiral excitations. We further show that the magnetoelectric effects in all phases disappear above a typical temperature corresponding to the total bandwidth of the effective fermionic model. To this end we explore the entropy, specific heat, magnetization, electric polarization, and the magnetoelectric tensor at finite temperature. We identify rather peculiar specific-heat and polarization behavior of the compass model which follows from highly frustrated interactions.

DOI: [10.1103/PhysRevB.90.094413](https://doi.org/10.1103/PhysRevB.90.094413)

PACS number(s): 75.10.Jm, 05.30.Rt, 75.25.Dk, 75.40.Cx

I. INTRODUCTION

In classical electromagnetism, electric (\vec{E}) and magnetic (\vec{H}) fields induce electric polarization (\vec{P}) and magnetization (\vec{M}) in matter, respectively, yet using \vec{H} (\vec{E}) to induce \vec{P} (\vec{M}), the so-called magnetoelectric effect (MEE), is a highly nontrivial issue [1]. Recently, technological and theoretical progress triggered a renaissance of the MEE, especially in multiferroic materials [2–5]. It was expected that the efficient control of magnetism in terms of the electric field would have many potential applications in spintronics and data-storage technology.

There are several envisaged explanations for the magnetically induced ferroelectricity. Among them, the exchange-striction mechanism [6,7] and the inverse Dzyaloshinskii-Moriya (DM) mechanism [8] are main streams in accounting for ferroelectricity in inversion-symmetry-breaking lattices. In the former mechanism, the bonds become different between the parallel and the antiparallel spins through exchange striction associated with symmetric superexchange ($\vec{\sigma}_i \cdot \vec{\sigma}_j$). As a result, the electric polarization \vec{P} is induced by the crystallographic deformations in the direction of the chain. Such a mechanism was originally introduced to explain the MEE in the material Cr_2O_3 [9] and was recently applied to other versatile systems [10–12].

Besides, for the noncollinear spiral or helimagnetic order, resulting from antisymmetric magnetic frustration, the term ($\vec{\sigma}_i \times \vec{\sigma}_j$) is also a common way to activate the inversion-symmetry breaking. The electric polarization \vec{P} is thereby generated by the displacement of oppositely charged ions as described by Tokura and Seki [13],

$$\vec{P}_i = \gamma \hat{e}_{ij} \times (\vec{\sigma}_i \times \vec{\sigma}_j), \quad (1.1)$$

where \hat{e}_{ij} is the unit vector connecting the neighboring spins $\vec{\sigma}_i$ and $\vec{\sigma}_j$. The coupling coefficient γ of the cycloidal component is material dependent [14], and its sign depends on the vector spin chirality. This microscopic origin towards magnetism-

induced ferroelectricity constitutes the well-known inverse DM mechanism. It was proposed that DM interaction induces the helimagnetic spin ground state and ferroelectricity in Cu_2OSeO_3 [15–17] and cycloidal magnetic structure in multiferroic BiFeO_3 [18]. Note, incidentally, that there is a plethora of experimentally accessible compounds where electron spin resonance can be applied as a consequence of the presence of DM interaction [19,20]. Meanwhile, a number of theoretical papers were devoted to the effects of DM interaction in magnets [21–24].

The concept of magnetism-driven ferroelectricity naturally brings significant attention to quantum spin systems. Among them, several spin-1/2 chain materials appear to be the most straightforward but conceptually important models and have been extensively studied, for example, $\text{Ca}_3\text{CoMnO}_6$ [6], LiCu_2O_2 [25], LiCuVO_4 [26], and CuCl_2 [27]. In a realistic quantum wire, the superexchange interaction between spins of transition metal ions depends on the details of crystal structure, such as the bond length between magnetic ions and the angle between the bonds connecting magnetic and ligand ions. The effect of such variants must be addressed.

So far most literature has focused on Heisenberg exchange interaction; such models require approximations and are not easy to solve completely. In order to obtain an unbiased solution we address in this paper the problem of ferroelectricity in the anisotropic exchange model which is exactly solvable. Our model is a generalization of the one-dimensional (1D) compass model where vector chiral correlations are introduced by the additional DM interaction. It features a rather rich phase diagram that results from the interplay of DM terms, external fields, and frustrated compass-type exchange interactions. We analyze the different symmetry breaking due to magnetic and electric fields. Further we demonstrate in the fermionic representation of the spin model that the gapless topological phase is characterized by four distinct Fermi points, in contrast to the conventional gapped phases or symmetry-protected

phases with twofold-degenerate Fermi points. We identify the nonlocal string order in the chiral phase accompanied by the finite electrical polarization. In particular we demonstrate the change of the entanglement spectrum between the canted Néel phase and the chiral phase.

The 1D compass model is a realization of the directional competing interactions known from the two-dimensional (2D) compass model [28–31] on a chain with alternating Ising-like interactions between x and z spin components on neighboring bonds. Similar to the Kitaev model [32,33], the 2D and 1D compass model are characterized by intrinsic frustration of interactions. An exact solution of the 1D compass model shows that the ground state has high degeneracy [34], and a quantum phase transition (QPT) occurs when anisotropic interactions pass through the isotropic point [35].

We have organized the paper into six sections. First, we introduce the Hamiltonian of the 1D generalized compass model (GCM) with DM interaction in Sec. II A and then present the procedure to solve it exactly by employing Jordan-Wigner transformation in the absence of magnetic field in Sec. II B. This solution is next used to evaluate various correlation functions at finite electric field in Sec. II C. The model in the magnetic field is analyzed in Sec. III, and the complete phase diagram is obtained when the electric and magnetic fields are varied. Several thermodynamic functions, such as the entropy and the specific heat, and the MEEs are presented and discussed in Secs. IV and V. Section VI contains the final discussion and conclusions.

II. THE 1D COMPASS MODEL AND ITS SOLUTION

A. From a frustrated magnet to spinless fermions

In this paper, we consider a frustrated 1D magnet with DM interaction, which relates to the magnetostriction and inverse DM (or spin-current) mechanisms in a nonstoichiometric structure. To focus attention, we assume that the 1D chain is along the x axis, i.e., $\hat{e}_{ij} = \hat{x}$, so the possible nonzero components of \vec{P}_i are P_i^y and/or P_i^z according to Eq. (1.1). In analogy to the 2D GCM [36], we consider interactions which interpolate between the Ising model and the frustrated interactions in the 1D compass model. Therefore we introduce an arbitrary angle $\pm\theta/2$ relative to σ_i^x for an odd/even bond, which defines new operators as linear combinations of $\{\sigma_i^x, \sigma_i^y\}$ spin components on even bonds,

$$\tilde{\sigma}_i(\theta) \equiv \cos(\theta/2) \sigma_i^x + \sin(\theta/2) \sigma_i^y, \quad (2.1)$$

with similar operators with angle $-\theta/2$ for odd bonds. In such frustrated systems, the Ising-like interactions along odd and even bonds have different strengths and preferential easy axes within the (σ^x, σ^y) plane along the chain of N sites.

The 1D GCM considered below is given by

$$\begin{aligned} \mathcal{H}_{\text{GCM}} = & \sum_{i=1}^{N'} \{J_o \tilde{\sigma}_{2i-1}(\theta) \tilde{\sigma}_{2i}(\theta) + J_e \tilde{\sigma}_{2i}(-\theta) \tilde{\sigma}_{2i+1}(-\theta)\} \\ & + \sum_{i=1}^N \{\vec{D}_i \cdot (\vec{\sigma}_i \times \vec{\sigma}_{i+1}) + \vec{E} \cdot \vec{P}_i + \vec{H} \cdot \vec{\sigma}_i\}, \quad (2.2) \end{aligned}$$

where J_o and J_e denote the coupling strength along odd and even bonds, respectively. For convenience an even number of sites $N = 2N'$ is assumed. Here \vec{E} is the electric field, and \vec{H} is the external magnetic field, which contains the g factor g and the Bohr magneton μ_B . \vec{D} is the DM vector, and the interaction comes from a relativistic correction to the usual superexchange that has a strength proportional to the spin-orbit coupling constant. Without an inversion center on any bond, the antisymmetric exchange is usually one order of magnitude smaller than the exchange interaction. An immediate question is to what extent they affect the nonmagnetic phase. Note that the first term in the Hamiltonian (2.2) interpolates between the 1D Ising model ($\theta = 0$) and the 1D compass model ($\theta = \pi/2$) [34,37,38]. At an intermediate value of $\theta = \pi/3$ the interactions correspond to e_g orbitals; such a model was recently introduced for a 1D zigzag chain in an (a, b) plane [35] and may be realized either in layered structures of transition metal oxides [39] or in optical lattices [40,41].

First, we consider below the model (2.2) in the absence of an external magnetic field. The role of magnetic field is explored in Sec. III. Without a magnetic field, the Hamiltonian is invariant under a rotation in spin space around the z axis and under time-reversal operator $\mathcal{T} = i\sigma_y K$, which reverses the sign of all spin-component operators. Here K denotes the complex conjugation operator, and σ_y is a Pauli matrix in spin space. As soon as a DM interaction is introduced, the Hamiltonian is no longer invariant with respect to a space inversion about a bond center. The DM interaction always induces an electric polarization according to Eq. (1.1) that lies within the rotation plane of the spins and is perpendicular to the magnetic bond and thus competes with the exchange energy. Here we presume that the \vec{D} vector is along the direction perpendicular to the plane, i.e., $\vec{D}_i = D^z \hat{z}$, and originates from symmetry breaking associated with the planar molecular structure that determines the (a, b) plane. In-plane components of the DM vector are assumed to be negligible compared with the out-of-plane components. By Eq. (1.1) an electric field component E^y along the in-plane y direction acts on the chiral polarization $(\vec{\sigma}_i \times \vec{\sigma}_{i+1})$ in the same way as the D^z component of the DM vector. Below we shall express this dependence, for the considered geometry, by the variable E , defined as

$$E = D^z + \gamma E^y. \quad (2.3)$$

The Hamiltonian (2.2) can be exactly diagonalized by following the standard procedures. The Jordan-Wigner transformation maps explicitly between spin operators and spinless fermion operators by the following relations [42]:

$$\begin{aligned} \sigma_j^+ &= \exp \left[i\pi \sum_{i=1}^{j-1} c_i^\dagger c_i \right] c_j = \prod_{i=1}^{j-1} \sigma_i^z c_j, \\ \sigma_j^- &= \exp \left[-i\pi \sum_{i=1}^{j-1} c_i^\dagger c_i \right] c_j^\dagger = \prod_{i=1}^{j-1} \sigma_i^z c_j^\dagger, \\ \sigma_j^z &= 1 - 2c_j^\dagger c_j, \end{aligned} \quad (2.4)$$

where c_j and c_j^\dagger are annihilation and creation operators of spinless fermions at site j , which obey the standard anticommutation relations: $\{c_i, c_j\} = 0$, $\{c_i^\dagger, c_j\} = \delta_{ij}$. Consequently,

we have a free-fermion Hamiltonian:

$$\hat{H}_E = \sum_i [J_o e^{i\theta} c_{2i-1}^\dagger c_{2i}^\dagger + (J_o - 2iE) c_{2i-1}^\dagger c_{2i} + J_e e^{-i\theta} c_{2i}^\dagger c_{2i+1}^\dagger + (J_e - 2iE) c_{2i}^\dagger c_{2i+1} + \text{H.c.}] \quad (2.5)$$

The spinless fermion Hamiltonian is equivalent to the 1D mean-field model for a triplet superconductor, with inhomogeneous nearest-neighbor hopping and condensate amplitudes [43].

B. Quasiparticles at finite electric field and $\vec{H} = 0$

The above Hamiltonian can be diagonalized; to this end we introduce the discrete Fourier transformation of the fermionic operators,

$$c_{2j-1} = \frac{1}{\sqrt{N'}} \sum_k e^{-ikj} a_k, \quad c_{2j} = \frac{1}{\sqrt{N'}} \sum_k e^{-ikj} b_k, \quad (2.6)$$

with the discrete momenta given as follows:

$$k = \frac{n\pi}{N'}, \quad n = -(N' - 1), -(N' - 3), \dots, (N' - 1). \quad (2.7)$$

The Hamiltonian takes the following form, which is suitable to introduce the Bogoliubov transformation:

$$\hat{H}_E = \sum_k [B_k a_k^\dagger b_{-k}^\dagger + A_k a_k^\dagger b_k - A_k^* a_k b_k^\dagger - B_k^* a_k b_{-k}]. \quad (2.8)$$

Here

$$\begin{aligned} A_k &= (J_o - 2iE) + (J_e + 2iE)e^{ik}, \\ B_k &= J_o e^{i\theta} - J_e e^{i(k-\theta)}. \end{aligned} \quad (2.9)$$

To diagonalize the Hamiltonian (2.8), we rewrite it in the Bogoliubov–de Gennes (BdG) form,

$$\hat{H}_0 = \sum_k \Gamma_k^\dagger \hat{M}_k \Gamma_k, \quad (2.10)$$

where

$$\hat{M}_k = \frac{1}{2} \begin{pmatrix} 0 & 0 & R_k + S_k & P_k + Q_k \\ 0 & 0 & P_k - Q_k & R_k - S_k \\ R_k^* + S_k^* & P_k^* - Q_k^* & 0 & 0 \\ P_k^* + Q_k^* & R_k^* - S_k^* & 0 & 0 \end{pmatrix} \quad (2.11)$$

and $\Gamma_k^\dagger = (a_k^\dagger, a_{-k}, b_k^\dagger, b_{-k})$. Here we have defined

$$\begin{aligned} P_k &= -i(J_e e^{ik} + J_o) \sin \theta, \\ Q_k &= (J_e e^{ik} - J_o) \cos \theta, \\ S_k &= J_o + J_e e^{ik}, \\ R_k &= 2iE(e^{ik} - 1). \end{aligned} \quad (2.12)$$

Within the Majorana representation, the BdG Hamiltonian (2.11) acts in an enlarged expanded Nambu-spinor space, namely, the tensor product of the physical space \mathbf{C}^{2N} with an extra degree of freedom \mathbf{C}^2 , which we call the ‘‘particle-hole space’’ [44]. This structure has an emergent particle-hole

symmetry (PHS) $\mathcal{C} = \tau_x K$, namely, $\{\hat{M}_k, \mathcal{C}\} = 0$. Here, τ_x is a Pauli matrix acting in the Nambu space. Note that both time-reversal operator \mathcal{T} and particle-hole transformation \mathcal{C} are antiunitary operators, satisfying $[\hat{H}, \mathcal{T}] = 0$, $\{\hat{H}, \mathcal{C}\} = 0$. As a consequence, two copies of the actual excitation spectrum, a particle and a hole copy, emerge simultaneously [45].

A unitary transformation \hat{U}_k can transform the Hermitian matrix (2.11) into a diagonal form,

$$\hat{Y}_k = \hat{U}_k \hat{M}_k \hat{U}_k^\dagger. \quad (2.13)$$

The quasiparticle (QP) operators, $\{\gamma_{k,1}^\dagger, \gamma_{k,2}^\dagger, \gamma_{k,3}^\dagger, \gamma_{k,4}^\dagger\}$, are connected with $\{a_k^\dagger, a_{-k}, b_k^\dagger, b_{-k}\}$ through the following relation:

$$\begin{pmatrix} \gamma_{k,1}^\dagger \\ \gamma_{k,4}^\dagger \\ \gamma_{k,2}^\dagger \\ \gamma_{k,3}^\dagger \end{pmatrix} = \hat{U}_k \begin{pmatrix} a_k^\dagger \\ a_{-k} \\ b_k^\dagger \\ b_{-k} \end{pmatrix}. \quad (2.14)$$

After diagonalization, the eigenspectra $\varepsilon_{k,j}$ ($j = 1, \dots, 4$) are readily obtained:

$$\varepsilon_{k,1(2)} = -\frac{1}{2} \sqrt{s_k \pm \sqrt{s_k^2 - \tau_k^2}}, \quad (2.15)$$

$$\varepsilon_{k,3(4)} = \frac{1}{2} \sqrt{s_k \mp \sqrt{s_k^2 - \tau_k^2}}, \quad (2.16)$$

where

$$\begin{aligned} s_k &= |P_k|^2 + |Q_k|^2 + |R_k|^2 + |S_k|^2, \\ \tau_k &= |P_k^2 - Q_k^2 - R_k^2 + S_k^2|. \end{aligned} \quad (2.17)$$

The eigenenergies are labeled sequentially from the bottom to the top as $\varepsilon_{k,1}, \dots, \varepsilon_{k,4}$ (see Fig. 1). Note that the spectra of mode $k = 0$ are independent of E , in contrast to the other modes. We can make this peculiarity to trace the order of the spectra. Instantly, we obtain the diagonal form of the

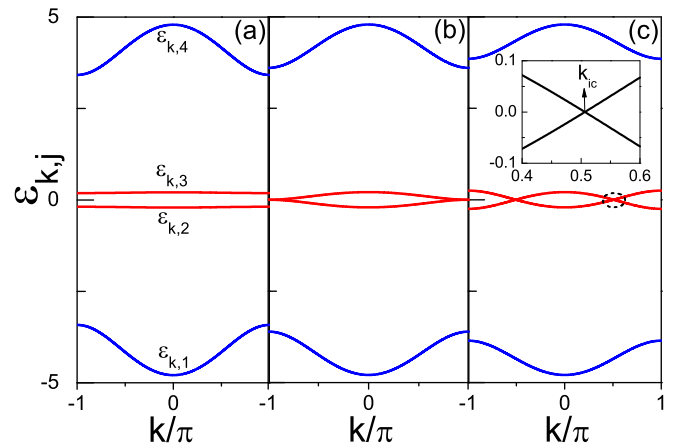


FIG. 1. (Color online) The energy spectra $\varepsilon_{k,j}$ ($j = 1, \dots, 4$) for increasing electric field E : (a) $E = 0.3$, (b) $E = 0.5$, and (c) $E = 0.7$. The inset in (c) is the amplification of the dashed circle below. Parameters are as follows: $J_o = 1$, $J_e = 4$, $\theta = \pi/3$, $H = 0$.

Hamiltonian,

$$\hat{H}_0 = \sum_k \sum_{j=1}^4 \varepsilon_{k,j} \gamma_{k,j}^\dagger \gamma_{k,j}. \quad (2.18)$$

One finds that the spectra are symmetric with respect to energy $\varepsilon = 0$ and the $k \leftrightarrow -k$ transformation; see the QP bands in Fig. 1. The positive spectra correspond to the electron excitations, while the negative ones are the corresponding hole excitations. As seen in Fig. 1(a), the upper two branches of the spectra, $\varepsilon_{k,3}$ and $\varepsilon_{k,4}$, are always positive for $E = 0.3$. The PHS implies here that $\gamma_{k,4}^\dagger = \gamma_{-k,1}$, $\gamma_{k,3}^\dagger = \gamma_{-k,2}$. Accordingly, the gap is determined by the absolute value of the difference between the second and third energy branches,

$$\Delta = \min_k |\varepsilon_{k,2} - \varepsilon_{-k,3}|. \quad (2.19)$$

With the increase of E , $\varepsilon_{\pi,3}$ bends down and $\varepsilon_{\pi,2}$ moves upwards at $k \approx \pm\pi$. Finally, $\varepsilon_{\pi,3}$ touches $\varepsilon_{\pi,2}$ at $E = 0.5$ and $k = \pm\pi$, i.e., $\Delta = 0$ [see Fig. 1(b)]. The condition for the gap closing requires $\tau_\pi = 0$, which gives rise to

$$E_c = \frac{1}{2} \sqrt{J_o J_e} |\cos \theta|. \quad (2.20)$$

Further increase of E leads to the bands inversion; $\varepsilon_{\pi,2}$ and $\varepsilon_{\pi,3}$ cross at two generally incommensurate and symmetric momenta $\pm k_{ic}$, which is given by

$$k_{ic} = \arccos \left(1 - \frac{J_o J_e \cos^2 \theta}{2E^2} \right). \quad (2.21)$$

One finds that in Fig. 1(c) the energies in the upper second band can be negative,

$$\varepsilon_{k,3} \leq 0 \quad \text{for} \quad |k| \geq k_{ic}. \quad (2.22)$$

The ground state of any fermion system follows the total filling of the Fermi-Dirac statistics, and the lowest energy is obtained when all the QP states with negative energies are filled by fermions. More precisely, in the thermodynamic limit ($N \rightarrow \infty$), the ground state of the system $|\Phi_0\rangle$ corresponds to the configuration with chemical potential $\mu = 0$, where all the states with $\varepsilon_{k,j} < 0$ are occupied and the ones with $\varepsilon_{k,j} \geq 0$ are empty. By means of the corresponding occupation numbers

$$n_{k,j} = \langle \Phi_0 | \gamma_{k,j}^\dagger \gamma_{k,j} | \Phi_0 \rangle = \begin{cases} 0 & \text{for } \varepsilon_{k,j} \geq 0, \\ 1 & \text{for } \varepsilon_{k,j} < 0. \end{cases} \quad (2.23)$$

One recognizes that in the present case of a symmetric QP spectrum, the ground-state energy may be expressed as

$$E_0 = -\frac{1}{2} \sum_k \sum_{j=1}^4 |\varepsilon_{k,j}|. \quad (2.24)$$

The advantage of the result given by Eq. (2.24) is that it is independent of the signs of J_o and J_e , which can be verified by transformations $\sigma_{2i-1}^x \rightarrow -\sigma_{2i-1}^x$ and $\sigma_{2i}^y \rightarrow -\sigma_{2i}^y$.

As observed in Fig. 2, the gap Δ diminishes after E exceeds the critical value E_c for a fixed angle θ ; E_c is symmetric with respect to $\theta = \pi/2$ and decreases with θ . As E approaches E_c (2.20) from below, the size dependence of the gap, $\Delta \sim L^{-z}$, defines the dynamic exponent z . Expanding

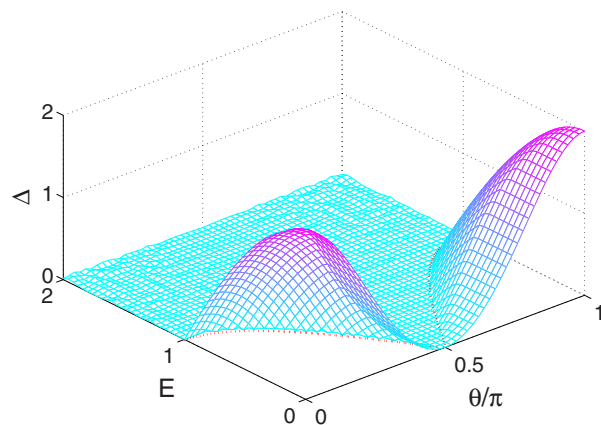


FIG. 2. (Color online) The gap Δ as a function of E and θ . The dotted lines are obtained from Eq. (2.20). They separate a gapless chiral phase from two gapful, canted Néel phases that are separated by a quantum critical point at $\theta = \pi/2$. Parameters are as follows: $J_o = 1$, $J_e = 4$.

the gap around the critical line E_c from lower threshold, i.e., at $\tau_k \rightarrow 0$,

$$\Delta \sim \frac{\tau_k}{\sqrt{2S_k}} \sim \frac{8(E_c^2 - E^2)}{\sqrt{J_o^2 + J_e^2}}. \quad (2.25)$$

The relativistic spectra at k_{ic} imply a dynamical exponent $z = 1$ for $\theta \neq \pi/2$ [see the inset in Fig. 1(c)]. The linear dispersion law guarantees that the density of low-energy states in the anisotropic chain remains finite instead of leading to the square-root divergence typical for isotropic spin chains [46]. In contrast, the point $\theta = \pi/2$ at $E = 0$ is a multicritical point with an emergent \mathbb{Z}_2 symmetry, and the spectra vanish quadratically at $\pm\pi$ as a result of the confluence of two Dirac points, corresponding to a dynamical exponent $z = 2$ [47].

C. Correlation functions

In order to characterize the QPTs, we study the nearest-neighbor correlation function,

$$C_l^\alpha = -\frac{2}{N} \sum_{i=1}^{N/2} \langle \sigma_i^\alpha \sigma_{i+l}^\alpha \rangle, \quad (2.26)$$

where the superscript $\alpha = x, y, z$ denotes a Cartesian component, and chirality,

$$X_l^\alpha = -\frac{2}{N} \sum_{i=1}^N \langle \vec{\alpha} \cdot (\vec{\sigma}_i \times \vec{\sigma}_{i+l}) \rangle, \quad (2.27)$$

where $\vec{\alpha}$ denotes the unit vector in the direction of a Cartesian component α . Finally, we introduce the nonlocal string order parameter,

$$O_s^\alpha = \langle S_{4k}^\alpha S_{4k+1}^\alpha S_{4k+2}^\alpha S_{4k+3}^\alpha \cdots S_{4n}^\alpha S_{4n+1}^\alpha S_{4n+2}^\alpha S_{4n+3}^\alpha \rangle. \quad (2.28)$$

The chirality X_l^α (2.27) will exhibit a sign change under the parity operation but will stay invariant under the time-reversal operation. It is well known that two-point correlation functions

can be calculated from determinants in terms of Wick's theorem [42,48],

$$\langle \sigma_0^x \sigma_r^x \rangle = \begin{vmatrix} G_{-1} & G_{-2} & \cdots & G_{-r} \\ G_0 & G_{-1} & \cdots & G_{-r+1} \\ \vdots & \vdots & \ddots & \vdots \\ G_{r-2} & G_{r-3} & \cdots & G_{-1} \end{vmatrix}, \quad (2.29)$$

$$\langle \sigma_0^y \sigma_r^y \rangle = \begin{vmatrix} G_1 & G_0 & \cdots & G_{-r+2} \\ G_2 & G_1 & \cdots & G_{-r+3} \\ \vdots & \vdots & \ddots & \vdots \\ G_r & G_{r-1} & \cdots & G_1 \end{vmatrix}, \quad (2.30)$$

$$\langle \sigma_0^z \sigma_r^z \rangle = 4 \langle \sigma_0^z \rangle \langle \sigma_r^z \rangle - G_r G_{-r}, \quad (2.31)$$

where

$$G_r = \langle \sigma_0^y \sigma_r^x \rangle. \quad (2.32)$$

When $E = 0$, the ground state is marked by the finite nearest-neighbor correlation functions, among which x components $\{C_i^x\}$ dominate for $\theta < \pi/2$, implying that the adjacent spins are antiparallel and aligned with a canted angle with respect to the x axis. In other words, the ground state of the GCM is a canted Néel (CN) phase for $\theta < \pi/2$. The predicted spin-wave spectrum can be compared with the results obtained from inelastic neutron scattering measurements [18,49]. Conversely, the z -component chirality X_i^z completely vanishes. With increase of E , C_i^x , C_i^y , and C_i^z remain unchanged until reaching a threshold value $E_c(\theta)$, as shown in Fig. 3(a). Simultaneously, the chiral order X^z starts to grow and saturates as $E \rightarrow \infty$. The DM interaction or the electric field induces spins to be cycloidally oriented in the (σ^x, σ^y) plane.

The effects of bond alternation and the DM interaction on the zero-temperature phase diagram of the Ising model have been studied in terms of an infinite time-evolving block decimation (iTEBD) algorithm [50]. The iTEBD method allows one to solve for the ground-state properties of a 1D translationally invariant spin system of infinite length. One of the main controlling factors under this strategy is the bond dimension χ , i.e., the cutoff dimension of Schmidt coefficients during the singular-value-decomposition process [51]:

$$|\Psi\rangle = \sum_{i=1}^{\chi} |\phi_i^L\rangle \Lambda_i |\phi_i^R\rangle, \quad (2.33)$$

where $|\phi_i^L\rangle$ and $|\phi_i^R\rangle$ represent the orthonormal bases of the subsystem to the left and right halves of the broken bond and Λ is a diagonal matrix. The iTEBD algorithm not only can reveal ground-state energy, excitations, and local correlation functions but also can conveniently evaluate nonlocal correlations, like quantum entanglement, which are not easy to obtain by other methods.

Quantum entanglement was originally introduced to exhibit nonlocal correlations in a quantum system [52–55]. Considering a d -dimensional block composed by L^d contiguous spins, embedded in an infinite system, the von Neumann entropy between the block and the rest of the system is given by

$$\mathcal{S}_L = -\text{Tr} \rho_L \log_2 \rho_L, \quad (2.34)$$

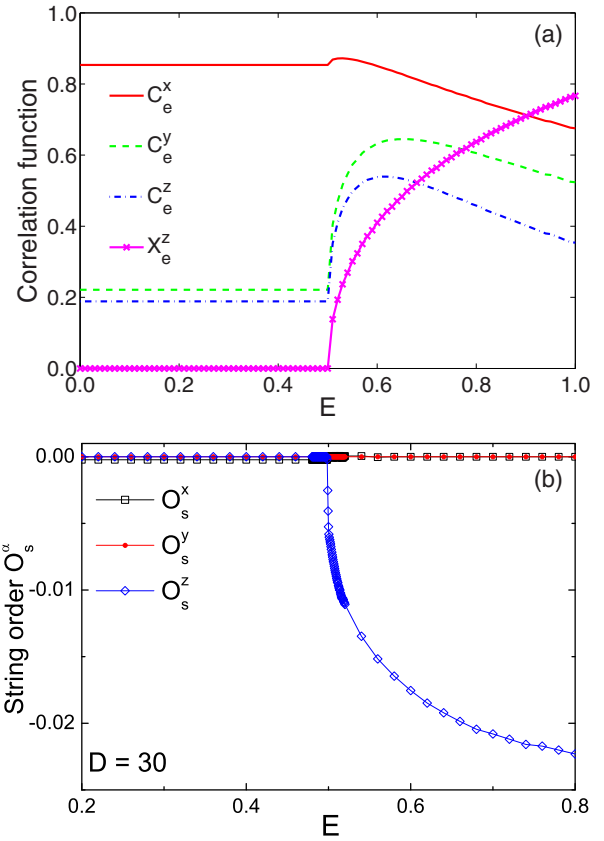


FIG. 3. (Color online) Evolution of the ground state for increasing electric field: (a) the nearest-neighbor correlations C^α and chirality X^α on even bonds; (b) the string order parameters O_s^α . The bond dimension is set as $\chi = 30$. Parameters are as follows: $n - k = 200$, $J_o = 1$, $J_e = 4$, $\theta = \pi/3$, and $H = 0$.

where ρ_L is the reduced density matrix for the L^d -site block. A celebrated boundary law is satisfied for

$$\mathcal{S}_L \sim L^{d-1} \quad (2.35)$$

in a gapped d -dimensional system due to a short-range correlation length [56,57], while a logarithmic additive term in gapless regimes becomes dominated by the form [58–62]

$$\mathcal{S}_L \sim \frac{c}{3} L^{d-1} \log_2 L, \quad (2.36)$$

where c is central charge. Moreover, the study of the entanglement spectrum, i.e., the eigenvalues ξ_i of the entanglement Hamiltonian H_L resulting from $\rho_L = e^{-H_L}$ [63], has recognized that the universal part of the entanglement spectrum reveals an intricate connection between a bulk property and edge physics [64].

An alternative way to look at the dimerization of a chain is via the study of entanglement entropy of weak and strong bonds [65]. In Fig. 4, the normalized entanglement spectra of the half-infinite chain, obtained by dividing the chain into two half-infinite chains, are shown as functions of E . Since Eq. (2.2) is a two-period system, we have two entanglement spectra (Λ^a and Λ^b) by cutting odd or even bonds. They are not equivalent; we find that the entanglement spectra Λ^b are doubly degenerate in chiral phases in contrast to Λ^a . The

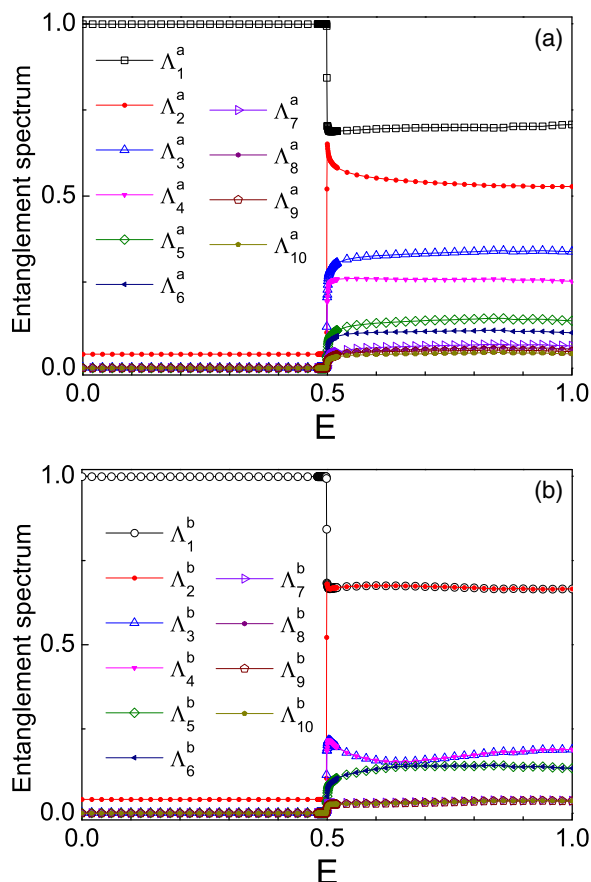


FIG. 4. (Color online) The normalized entanglement spectrum for increasing electric field E by cutting (a) a single odd bond and (b) a single even bond. Parameters are as follows: $J_o = 1$, $J_e = 4$, $\theta = \pi/3$, and $H = 0$.

exact twofold degeneracy in the entire entanglement spectrum is protected by the space inversion (parity) symmetry of the “odd-parity” chiral state [66], and this implies the existence of a nonlocal string order parameter [67]. The iTEBD calculation reveals that nonlocal correlation O_s^z arises for $E > E_c$, as observed in Fig. 3(b). The bipartite entanglement between two half-infinite chains can be directly read out through

$$S_{2i-1,2i} = -\text{Tr}[(\Lambda^a)^2 \log_2(\Lambda^a)^2], \quad (2.37)$$

$$S_{2i,2i+1} = -\text{Tr}[(\Lambda^b)^2 \log_2(\Lambda^b)^2]. \quad (2.38)$$

The bipartite entanglement on even bonds is larger than that on odd bonds, and both of them exhibit a singularity at criticality. In the iTEBD calculation the divergence of S_{vN} at the critical point is argued to scale with bond dimension χ as [68]

$$S_{\text{vN}} \sim \frac{1}{\sqrt{12/c} + 1} \ln \chi. \quad (2.39)$$

A QPT is indicated to exist in the zero-temperature phase diagram by nonanalyticity of order parameters with the controlling parameter. Thus, one finds a QPT from the gapped Néel phase to the gapless chiral phase at the critical point E_c . The three-dimensional phase diagram as functions of varying

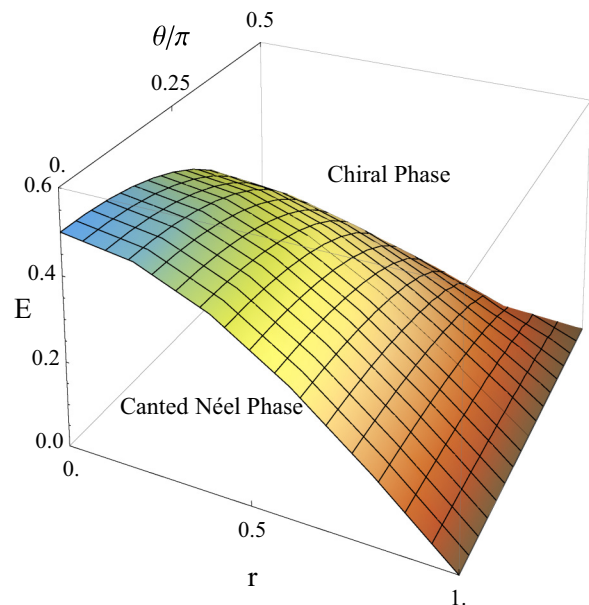


FIG. 5. (Color online) Ground-state phase diagram of Eq. (2.2), at zero magnetic field, as a function of the dimerization parameter [Eq. (2.40)], the electric field E , and angle θ .

angle θ , dimerization parameter

$$r \equiv \frac{J_e - J_o}{J_e + J_o}, \quad (2.40)$$

and electric field E is presented in Fig. 5. The transition from the CN phase to the chiral phase occurs at the critical value of the electric field E_c given by Eq. (2.20). The CN phase is stable in a finite range of $0 < E < E_c$, except for the limit of decoupled dimers on even bonds ($r = 1$), or the value of $\theta = \pi/2$, where the chiral phase exists at any electric field strength E .

Until now we have focused on the role played by the DM interaction and the applied electric field in the model. It is of interest now to ask how the above scenario is modified by the additional effect of finite magnetic field, and we explore this problem in the following section.

III. GENERALIZED COMPASS MODEL IN A HOMOGENOUS MAGNETIC FIELD

Here we study the effect of a homogenous magnetic field and the associated MEEs. We consider the case where the magnetic field is oriented perpendicular to the easy plane of the spins, i.e., $\vec{H} = H\hat{z}$. Subsequently, in Nambu representation, the Hamiltonian matrix is modified in the following way:

$$\hat{M}_k \rightarrow \hat{M}'_k = \hat{M}_k - H\mathbb{I}_2 \otimes \sigma^z, \quad (3.1)$$

where \mathbb{I}_2 is a (2×2) unity matrix. The directional Zeeman splitting perpendicular to the (x, y) plane lifts the Kramers degeneracy and makes the expression for the ground-state energy rather involved, which will not be shown here. The analytical solution of Hamiltonian (3.1) along the path $E = 0$ had been scrutinized recently, and an order-disorder QPT induced by the magnetic field was recognized [35]. Such criticality is suited at momentum $k = 0$. Generally, the

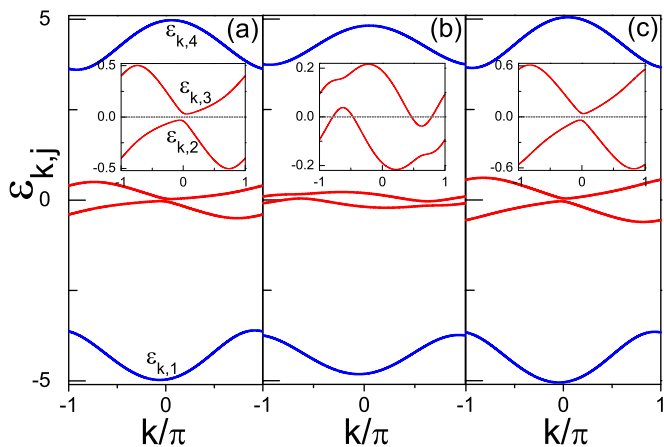


FIG. 6. (Color online) The energy spectra $\varepsilon_{k,j}$ ($j = 1, \dots, 4$) for (a) the CN phase at P_1 ($E = 0.3, H = 1.8$), (b) the chiral phase at P_2 ($E = 0.6, H = 0.6$), and (c) the polarized phase at P_3 ($E = 0.2, H = 2.2$). Insets show the amplification of the corresponding two central branches. $\varepsilon_{k,3}$ is negative for $k \in (0.4655\pi, 0.7871\pi)$ at P_2 . A horizontal guiding line marks the position of the chemical potential, i.e., $\mu = 0$. Parameters are as follows: $J_o = 1, J_e = 4, \theta = \pi/3$.

Hamiltonian (2.2) breaks the space-inversion symmetry of the spin chain when electric field E is applied, while the H field breaks the time-reversal symmetry (TRS). Figure 6 shows the energy spectra for three typical values of E and H . The joint breaking of TRS and parity symmetry leads to the asymmetry of the bands with respect to $k = 0$.

The BdG band structure in the absence of further symmetries still preserves the antiunitary PHS. The PHS of the BdG Hamiltonian is

$$\mathcal{C}\hat{M}_k\mathcal{C} = -\hat{M}_{-k}. \quad (3.2)$$

Hence, we have

$$\varepsilon_{k,1} = -\varepsilon_{-k,4}, \quad \varepsilon_{k,2} = -\varepsilon_{-k,3}. \quad (3.3)$$

Note that $k = 0$ and $k = \pm\pi$ are special points; the latter are called “time-reversal-invariant” points since they are mapped onto themselves. At $E = 0.6$ and $H = 0.6$, we can see from Fig. 6(b) that the energy spectrum $\varepsilon_{k,3}$ is not positive for all k values in the Brillouin zone, as this band crosses from positive to negative values at some intermediate value of k . The appearance of hole and electron pockets generate four Fermi points and is the key feature of the chiral phase at finite H field. A scrutiny of gap for typical parameters in Fig. 7 incorporating Lee-Yang zeros [69–71] shows three different phases. Two of them are gapped in the excitation spectrum, while the third one is gapless.

The spin chirality ($\vec{\sigma}_i \times \vec{\sigma}_{i+1}$) is perpendicular to the spin-spiral plane and is odd under spatial reflections. The magnetic field $\propto H$ induces a tilt of the spin-spiral plane. Both the time-reversal and parity symmetries are broken in this spin-spiral phase. As a result, it exhibits a MEE and thus leads to a directional change of polarizations P and staggered magnetic moments, which can be measured by nuclear magnetic resonance (NMR) and muon spectroscopy (μ SR) [72].

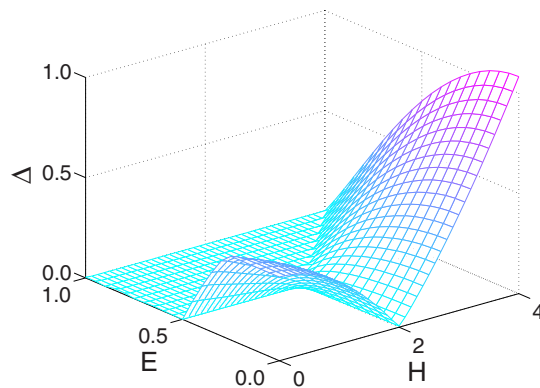


FIG. 7. (Color online) The excitation gap Δ as functions of electric (E) and magnetic (H) fields. One recognizes the gapped CN (polarized) phase at small (large) H and the gapless chiral phase at large E . Parameters are as follows: $J_o = 1, J_e = 4, \theta = \pi/3$.

The corresponding components of magnetization are shown in Fig. 8 for increasing H . The magnetization is found to be almost independent of E as long as the system is within a given magnetic phase, but discontinuous changes of magnetization occur at phase transitions. At $E = 0.3$, an abrupt change of each σ_i^α component occurs at $H = 2.0$, and only the z component of the magnetization survives for

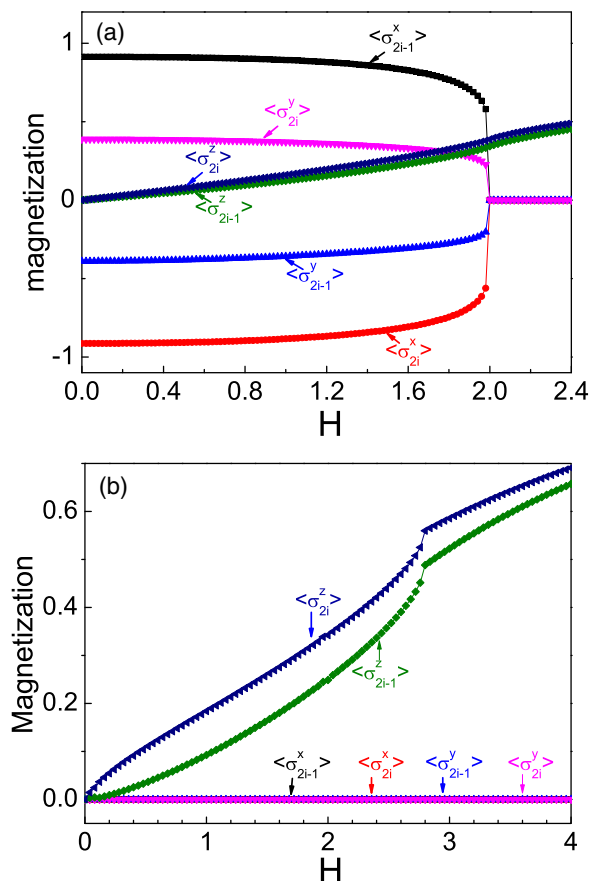


FIG. 8. (Color online) Evolution of magnetization components with magnetic field H for (a) $E = 0.3$ and (b) $E = 0.7$. Parameters are as follows: $J_o = 1, J_e = 4, \theta = \pi/3$.

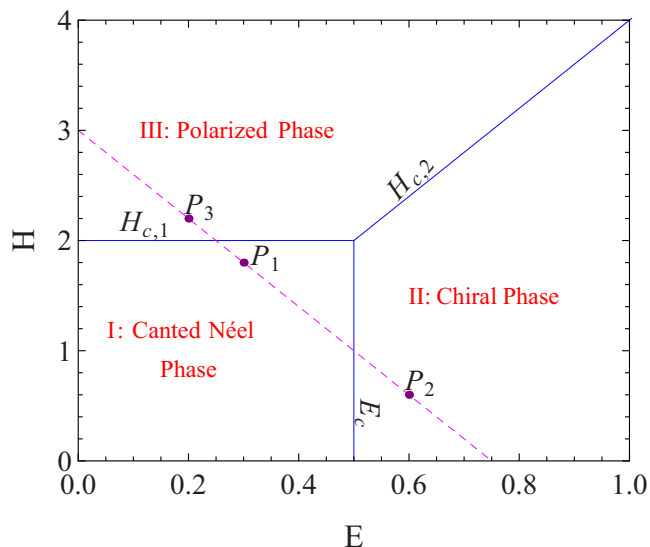


FIG. 9. (Color online) Magnetic phase diagram of the 1D GCM at $\theta = \pi/3$ with three critical lines, $H_{c,1}$, $H_{c,2} = 4E$ and E_c . In the special case $\theta = \pi/2$, there will no longer be a CN phase. The magenta dashed line denotes a typical path, $H = 3 - 4E$, that will be used in the following discussion. Parameters and the representative points $\{P_1, P_2, P_3\}$ in the (E, H) plane are defined in Fig. 6.

$H > 2.0$ [see Fig. 8(a)]. A nonzero chirality X_i^z shows up when $H > 2.0$. At $E = 0.7$, the x th and y th magnetization components completely disappear regardless of the value of H [see Fig. 8(b)]. Only the z th magnetization component is monotonously enhanced by increasing magnetic field, and a discontinuity occurs at $H = 2.8$. The sharp downturn of the magnetization below the critical field indicates a competition with the chiral order parameter of the chiral phase, and the chirality X_i^z decreases as H grows and a kink also arises at $H = 2.8$. A remarkable finding is that local magnetizations of each sublattice are not uniform under the competition of E and H ; that is, $|\langle \sigma_{2i-1}^x \rangle|$ is slightly larger than $|\langle \sigma_{2i}^x \rangle|$, while $|\langle \sigma_{2i-1}^y \rangle|$ and $|\langle \sigma_{2i-1}^z \rangle|$ are smaller than their counterparts. The ferrimagnetic structure is observed in some magnetoelectric materials, such as hexaferrites $\text{Ba}_{0.5}\text{Sr}_{1.5}\text{Zn}_2\text{Fe}_{12}\text{O}_{22}$ [73] and $\text{Ba}_2\text{Mg}_2\text{Fe}_{12}\text{O}_{22}$ [74].

Following all the criteria, including correlators, chirality, the string order parameter, the entanglement spectrum, and fidelity, the phase diagram in the (E, H) plane is displayed in Fig. 9. For relatively small H and E one finds region I, which corresponds to the CN phase, limited by two critical lines at $E = E_c$ and $H = H_{c,1}$. The critical lines are defined by

$$H_{c,1} = 2\sqrt{J_o J_e} |\cos \theta|, \quad (3.4)$$

$$E_c = \frac{1}{2}\sqrt{J_o J_e} |\cos \theta|. \quad (3.5)$$

The area of the CN phase is proportional to $\cos^2 \theta$ and shrinks to a point at $\theta = \pi/2$. While $E > E_c$, we find the third critical line,

$$H_{c,2} = 4E, \quad (3.6)$$

which separates the chiral phase at low magnetic field from the polarized phase at high magnetic field.

The long-range order is spoiled beyond the CN phase. Numerical results show that S_L saturates to a constant (2.35) in CN and a polarized phase, and a logarithmic divergence (2.36) with $c = 1/2$ is observed along the critical line $H_{c,1}$, suggesting the QPT belongs to the 2D Ising universality class. Specifically, S_L also displays a logarithmic form in the chiral phase; however, $c = 1$ is confirmed, implying that the QPT to chiral phase falls within the well-known 1D XX universality class. The logarithmic boundary-law violation is attributed to its gapless nature. The gapless character will have a considerable impact on the thermodynamic properties as any minor thermal fluctuation should intermix the ground state and excited states.

IV. THERMODYNAMIC PROPERTIES

The remainder of the paper is concerned with the case where the system is in thermal equilibrium. It is straightforward to obtain the thermodynamic characteristics of the model (2.2) at finite temperature. The free energy per site of the quantum spin chain at temperature T is equal to

$$\mathcal{F} = -\frac{T}{N} \sum_k \sum_{j=1}^4 \ln \left(2 \cosh \frac{\epsilon_{k,j}}{T} \right). \quad (4.1)$$

Here we use the units with the Boltzmann constant set as $k_B \equiv 1$. We derive the entropy, which is arguably a fundamental thermodynamic quantity and has been considered at low temperature for a long time [75]. We obtain the entropy \mathcal{S} and the specific heat C_V from the free energy \mathcal{F} via the standard relations:

$$\mathcal{S} = -\frac{\partial \mathcal{F}}{\partial T}, \quad (4.2)$$

$$C_V = -T \frac{\partial^2 \mathcal{F}}{\partial T^2}. \quad (4.3)$$

As we show in Fig. 10(a), the entropy at low temperatures displays two local maxima, implying two successive QPTs with the increase of electric field E . One is close to $E = 0.25$, and the other is located at $E = 0.5$. From the conformal field theory (CFT), the low-temperature expansion of the free energy of the chiral phase per site is given by [76–78]

$$\mathcal{F} = \epsilon_0 - \frac{\pi c}{6v_F} T^2 + O(T^3), \quad (4.4)$$

where ϵ_0 is the ground-state energy per site and v_F is the velocity of the excitations. Consequently, a linear relation of \mathcal{S} with T is observed in the gapless chiral phase with scaling [79],

$$\mathcal{S} = \frac{\pi c}{3v_F} T. \quad (4.5)$$

Here we adopt the units of $\hbar \equiv 1$.

The theoretical description of the chiral phase should be applicable for the whole gapless regime in 1D systems. In this respect, the system is gapless along the critical line, and its entropy is also linear in T , i.e., $\mathcal{S}(T) \propto T$, in the regime of low temperature, while in the gapped phases an exponential scaling is observed, i.e., $\mathcal{S} \propto \exp(-\Delta/T)$ [see Fig. 10(b)].

In fact, either in the chiral phase or at critical lines, the low-temperature thermal entropy and the universal part of the entanglement entropy are linked by a universal scaling function in the framework of the 1D CFT since both of them stem from the low-energy degrees of freedom close to the Fermi surface. The dynamical critical exponent z controls the relative scaling of space and temperature, leading to an invariant form $LT^{1/z}$. For 1D relativistic scale-invariant systems the finite-temperature fluctuations behave like $(LT)^d$. Here we set $z = d = 1$. On the one hand, the von Neumann entropy recovers the usual entanglement entropy of the ground state as $LT^{1/z} \rightarrow 0$, and only constant or logarithmic terms are allowed at $T = 0$. A lot of studies revealed that the coefficient of the boundary-law term (2.35) is nonuniversal, but the boundary-law-violating term (2.36) at zero temperature was proven to be universal. On the other hand, in the opposite limit as $LT \rightarrow \infty$, the dimensionlessness and extensivity require that the thermal entropy per site then scale linearly with T [80].

The specific heat C_V of the GCM in the transverse field has been plotted in Fig. 11(a). For extremely low temperatures, the specific heat presents a broad peak around the critical point and reaches a local minimum on the top of the peak at quantum critical points (QCPs). In the gapped phase, the low-temperature specific heat reveals an exponential increase in T in the absence of spontaneous magnetization. Since $C_V = T(\partial S/\partial T)$, the specific heat at the QCPs is identical to its entropy. In particular, the specific heat $C_V(T)$ of the Luttinger liquid is also linear in T [81].

A special case is the quantum compass model (QCM) realized at $\theta = \pi/2$. Here we find that the low-temperature

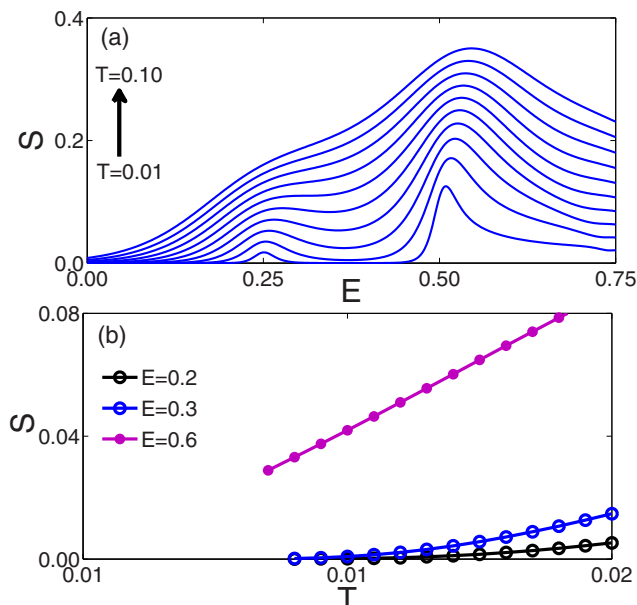


FIG. 10. (Color online) Entropy S of the 1D e_g orbital model at finite electric field and temperature: (a) the entropy vs electric field at increasing temperature $T = 0.01, 0.02, \dots, 0.10$ (from bottom to top) along the path $H = 3 - 4E$ defined in phase diagram shown in Fig. 9; (b) scaling of entropy $S(T)$ as a function of temperature T for critical (solid circles) and noncritical (open circles) fields. Parameters are as follows: $J_o = 1$, $J_e = 4$, $\theta = \pi/3$.

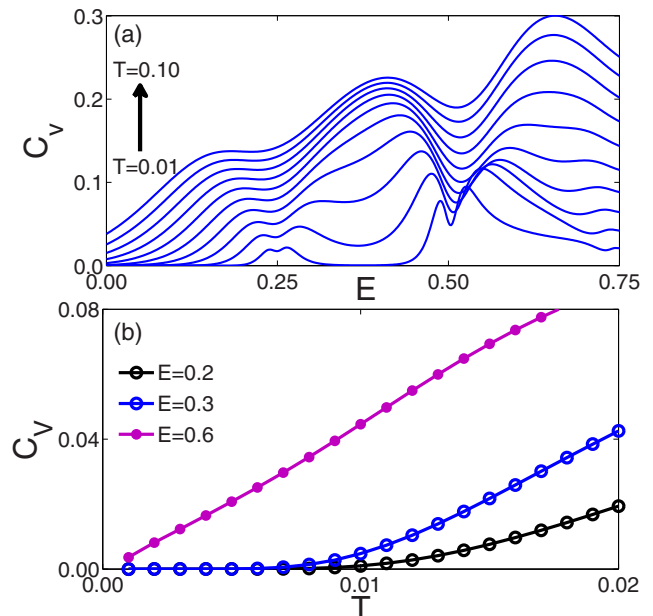


FIG. 11. (Color online) Specific heat C_V of the 1D e_g orbital model as function of electric field and temperature. (a) The specific heat vs electric field along the path $H = 3 - 4E$ at different temperatures $T = 0.01, 0.02, \dots, 0.10$ (from bottom to top); the specific heat reaches its local minimums at QCPs for extremely low temperatures. (b) The scaling of specific heat at local minimum with respect to T . Parameters are as follows: $J_o = 1$, $J_e = 4$, $\theta = \pi/3$.

behavior is non-Fermi-liquid-like and remarkably different from the behavior obtained at other values of θ . The entropy at different temperatures is plotted as a function of the E field in Fig. 12(a) along the critical line $H = 4E$, which extends here to $E = 0$. We recall that for $\theta = \pi/2$ the CN phase has disappeared. Usually, according to the third law of thermodynamics, the entropy falls to zero at $T \rightarrow 0$. Here it approaches the maximal value $S = \ln 2$ per unit cell for a small E field in the low- T limit, as a result of the macroscopic degeneracy $2^{N/2-1}$ in the disordered state [82]. Large residual entropy was measured in the spin-ice system $\text{Dy}_2\text{Ti}_2\text{O}_7$ [83], where it is related to a macroscopic degeneracy of the ground state resulting from frustration in the pyrochlore lattice.

The measurement of the full magnetic field and temperature dependence of the complete entropic landscape was performed for $\text{Sr}_3\text{Ru}_2\text{O}_7$ near quantum criticality [84]. Lowering the entropy of ultracold gases becomes nontrivial to realize more exotic quantum states [85–87], such as d -wave superconductivity. Simultaneously, the specific heat remains zero for vanishing field, as shown in Fig. 12(b). This follows from the excitation gap, which opens at this value of θ between the degenerate ground state and excited states.

V. MAGNETOELECTRIC EFFECTS

The advantage of the presented formalism is that the magnetization, the electric polarization, and thereby the magnetoelectric tensor can be calculated exactly for the entire temperature range relevant for the phase diagram. Figure 13

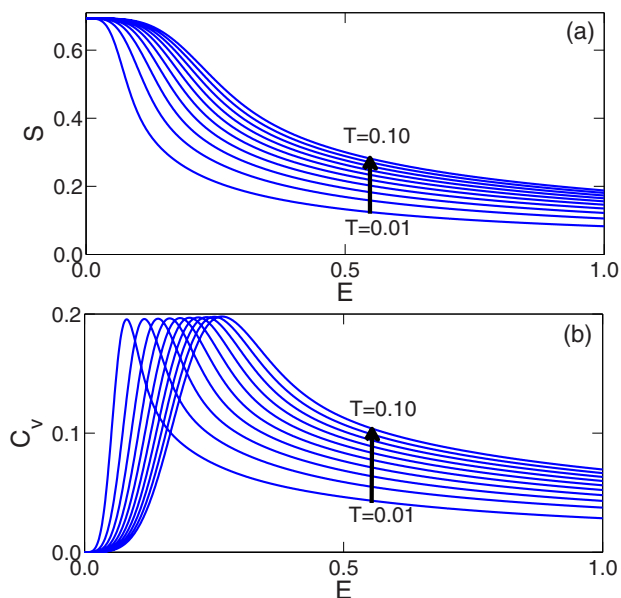


FIG. 12. (Color online) Thermodynamic properties of the QCM for increasing electric field E as obtained along the phase boundary $H = 4E$: (a) the entropy \mathcal{S} and (b) the specific heat C_V . Different lines are for increasing temperature $T = 0.01, 0.02, \dots, 0.10$ (from bottom to top at $E = 0.5$). Parameters are as follows: $J_o = 1$, $J_e = 4$, $\theta = \pi/2$.

shows the average magnetization,

$$M^z = \frac{1}{N} \sum_l \langle \sigma_l^z \rangle, \quad (5.1)$$

and the electric polarization,

$$P^y = \frac{1}{N} \sum_l \langle \sigma_l^x \sigma_{l+1}^y - \sigma_l^y \sigma_{l+1}^x \rangle, \quad (5.2)$$

as functions of the magnetic field H for a few selected values of the electric field E at very low temperatures. Here the angle brackets $\langle \dots \rangle$ denote the thermal average.

A key quantity to characterize the MEE is the linear magnetoelectric susceptibility at constant temperature. The numerical derivatives of P^y and M^z with respect to H and E define the magnetoelectric tensor α^{yz} ,

$$\alpha^{\mu\nu} = - \left(\frac{\partial P^\mu}{\partial H^\nu} \right)_{T, \vec{E}} = - \left(\frac{\partial M^\nu}{\partial E^\mu} \right)_{T, \vec{H}}. \quad (5.3)$$

The size of the macroscopic MEE depends on the microscopic mechanism. Below we use the abbreviation α for the magnetoelectric tensor component α^{yz} .

In Fig. 13(a) the electric polarization P^y is large in the chiral phase (the case of $E = 0.7$), and it decreases strongly towards the phase transition to the polarized phase at $H = H_{c,2}$. In contrast, in the CN phase (at $E = 0.3$) P^y starts from zero and increases gradually with H but remains small compared to the chiral phase. Actually, we find that the polarization P^y behaves quadratically at small $H \simeq 0$ in the CN phase and shows a gradual decrease after entering the polarized phase. In the limit of large H the polarization decreases again to zero.

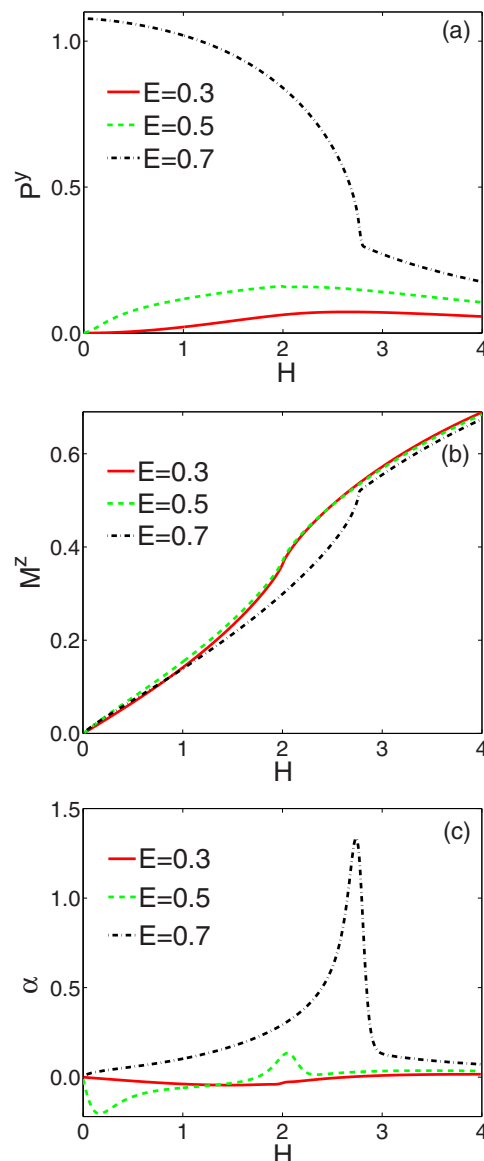


FIG. 13. (Color online) Evolution of various quantities with increasing magnetic field H at low temperature $T = 0.01$ and three values of electric field, $E = 0.3, 0.5, 0.7$ (see legend): (a) y -direction electric polarization P^y , (b) z -component magnetization M^z , and (c) the magnetoelectric tensor α through relation $\partial_H P^y$. Parameters are as follows: $J_o = 1$, $J_e = 4$, and $\theta = \pi/3$.

In the CN phase the M^z component of the magnetization [Fig. 13(b)] grows with E and reaches a maximum at the critical line E_c , which is contrary to the trend found at the critical line $H_{c,2}$ (not shown). Figure 13(b) reveals the S-shaped continuous variation of the magnetization M^z at the phase transition between the CN and polarized phases, i.e., for $E = 0.3$ and also for $E = 0.5$. In contrast, the transition at $E = 0.7$ appears as a second-order phase transition, where the M^z order is suppressed below $H_{c,2}$ by the appearance of the chiral order and the associated strong variation of P^y . This naturally leads to a huge signal in the MEE tensor component α , as seen in Fig. 13(c) for $E = 0.7$. On the other hand, α remains small in the CN and polarized phases at $E = 0.3$ but

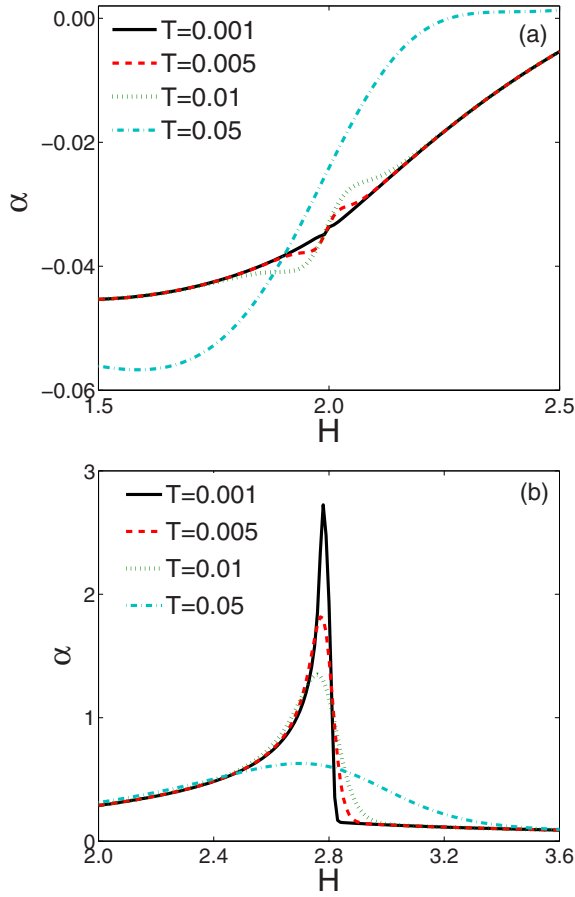


FIG. 14. (Color online) Magnetolectric tensor α as a function of H obtained for (a) $E = 0.3$ and (b) $E = 0.7$ close to the critical point. The square-root singularity at $T = 0$ decays rapidly with increasing temperature. Parameters are as follows: $J_o = 1$, $J_e = 4$, and $\theta = \pi/3$.

develops strong features at $E = 0.5$ both at small H and in the vicinity of H_c .

In Fig. 14 we compare the magnetic field dependence of the magnetolectric tensor α at different temperatures T . It is evident that also the variation with temperature distinguishes (i) the phase transition from the CN phase to the polarized phase and (ii) the transition from the chiral phase to the polarized phase. In Fig. 14(a) the magnetolectric tensor undergoes a gradual change at $E = 2.0$ for $E = 0.3$ under extremely low temperature. α manifests opposite trends on both sides of the critical point as the temperature increases. Increasing temperature suppresses α in the polarized state, while enhancing it in the CN phase. Remarkably, α displays van Hove-like singularities close to $H_{c,2} = 2.8$ for $E = 0.7$. These singularities gradually disappear at increasing temperature, and one finds that α becomes more and more flat, as shown in Fig. 14(b). We have found that the singular behavior is smeared out when $T > 0.05$.

The temperature dependence of P^y , M^z , and α is displayed in Figs. 15(a)–15(c). The data are shown at three points, P_1 , P_2 , and P_3 , representing the CN phase, the chiral phase, and the polarized phase, respectively (see the phase diagram of Fig. 9). In Fig. 15(a) we find that the P^y component of the electric polarization for point P_2 saturates at its maximal value at low

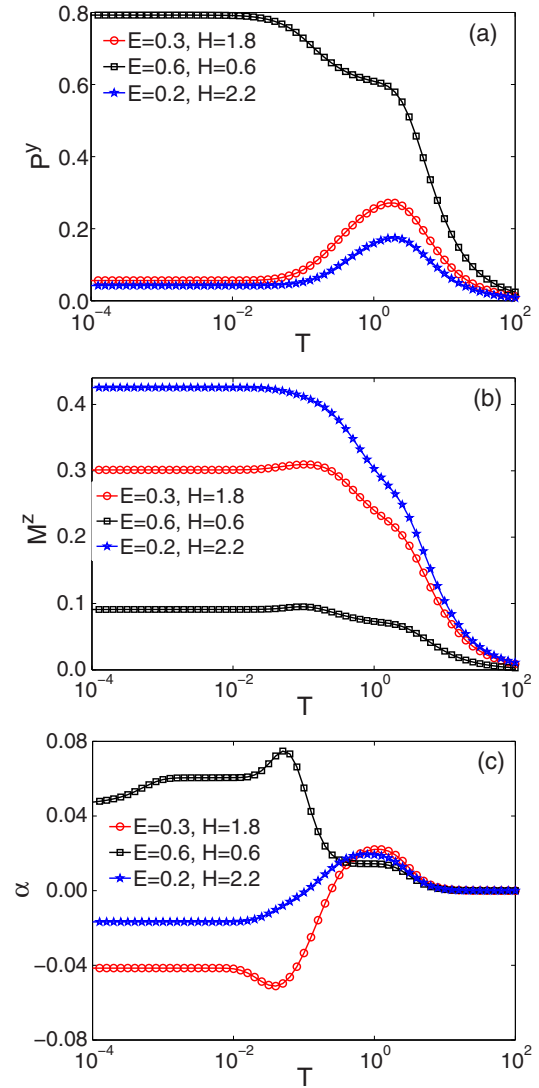


FIG. 15. (Color online) Temperature dependence (note the logarithmic scale) of the magnetolectric effect for three selected (E, H) points, $P_1 \equiv (0.3, 1.8)$, $P_2 \equiv (0.6, 0.6)$, and $P_3 \equiv (0.2, 2.2)$, corresponding to the CN, chiral, and polarized phases, respectively: (a) the polarization P^y , (b) magnetization M^z , and (c) magnetolectric tensor α . Parameters are as follows: $J_o = 1$, $J_e = 4$, and $\theta = \pi/3$.

temperatures. With increasing temperature $P^y(T)$ decreases in two steps: (i) the first decrease at $T_1 \sim 0.1$ can be identified with the excitation energy between the chiral low-energy states and nonchiral excited states, while (ii) the final decay of $P^y(T)$ towards zero at $T_2 \sim 10$ can be related to the total range of excitation energies.

Interestingly, the two characteristic temperature scales are also recognized in the other phases. In the polarized and CN phases $P^y(T)$ increases above T_1 from very small values at low temperatures and assumes relatively large values near $T \sim 1$, i.e., comparable to those in the chiral phase, and becomes small above T_2 . Surprisingly, the magnetolectric effects are of similar strength in all three magnetic phases in the intermediate temperature regime, $T_1 < T < T_2$.

The same two characteristic temperatures may be recognized in the temperature dependence of the magnetization

$M^z(T)$ and magnetoelectric tensor $\alpha(T)$. The magnetoelectric tensor α changes sign from negative to positive values upon increasing temperature, reflecting the maximum in $P^y(T)$ within the polarized and CN phases. The derivative $(\partial M^z/\partial T)$ also changes its sign at T_1 . We note that T_1 decreases monotonously when approaching the chiral phase along the path depicted in Fig. 9, and the reentrant behavior of P^y vanishes after entering the chiral phase.

VI. DISCUSSION AND CONCLUSIONS

In this paper we have considered the 1D generalized compass model which interpolates between the Ising model ($\theta = 0$) and the maximally frustrated QCM ($\theta = \pi/2$) via the e_g orbital model and includes Dzyaloshinskii-Moriya interaction. We investigated this model in the presence of external magnetic and electric fields. The Ising-like exchange interactions are directional in the compass model, and we selected the preferential axes in such a way that interactions lie within the (σ^x, σ^y) plane. The particular advantage of the presented model is that it can be solved exactly in terms of Jordan-Wigner transformation, and therefore the magnetization, correlation functions, and the phase diagram could be obtained rigorously. Note that, usually, the effective Ising interactions have to be treated in the mean-field approximation, which is uncontrolled.

The analytical results show that the angle θ between the easy axes on odd and even bonds plays a crucial role in determining the properties of the generalized compass model, including intersite spin correlations and the excitation gap. We have shown that for $\theta = \pi/3$, corresponding to the e_g orbital model, the 1D model is in the same universality class as the Ising model, whose ground state is Néel ordered. The presence of coplanar staggered $\langle \sigma_i^{x(y)} \rangle$ order in this phase opens the possibility for the existence of transverse order in addition. Indeed, the magnetic field polarizes the system into ferromagnetic alignment. These two phases exhaust the phase diagram at vanishing (or small) electric field.

In contrast, finite electric field drives the system into a chiral phase, which is characterized by nonlocal z th-component string order. The development of such a peculiar phase can be regarded as a spontaneous generation of Dzyaloshinskii-Moriya interaction, which breaks the parity symmetry and exhibits a magnetoelectric effect. We have demonstrated that the entanglement spectra of a half-infinite chain as a function of electric field may also be used to determine the phase diagram. Both Néel and polarized phases are gapped, where entanglement is a constant satisfying the boundary law, while entanglement in the gapless chiral state shows a logarithmic divergence.

By analyzing the exact results at finite temperature obtained for entropy and specific heat, we have established that the thermal properties exhibit anomalies in the vicinity of quantum critical points. As a function of the electric field, the entropy displays local maxima, while the specific heat exhibits local minima at critical points for extremely low temperature, where a linear scaling with temperature was established. Away from the quantum critical point, exponential decay of the entropy and specific heat with the inverse temperature is observed instead of a linear dependence on T in the chiral phase.

The QCM is a very special case, which is realized at the angle $\theta = \pi/2$, for which the spin components of the exchange interactions along the even/odd bonds are orthogonal. The QCM represents a peculiar quantum critical state between two gapped phases. Removing external fields, i.e., at $E = 0$ and $H = 0$, the low-energy elementary excitations in Eq. (2.16) become dispersionless and tend to zero energy, i.e., $\varepsilon_{k,2} = \varepsilon_{k,3} = 0$. This flat band is then half filled by fermions and thus gives high macroscopic degeneracy $2^{N/2-1}$ away from the isotropic point and the increased degeneracy of $2^{N/2}$ when the spin interactions are balanced (at $J_o = J_e$). The degeneracy for isotropic spin interactions increases further by a factor of 2 in the thermodynamic limit, being $2 \times 2^{N/2}$.

The critical lines intersect at $\theta_c = \pi/2$, $H_{c,1} = 0$, $E_c = 0$, forming a multicritical point. The phase diagram changes qualitatively in this case. The $z = 2$ critical Fermi surface corresponds to a marginal Fermi liquid, and it has a nonzero entropy density as $T \rightarrow 0$. This indicates the absence of Néel-like long-range order in the ground state of the $\theta = \pi/2$ compass model. A finite magnetic field opens an exponentially small gap at the Fermi energy and thus removes the high degeneracy of the ground state. However, applying the Dzyaloshinskii-Moriya-type electric field, the spectra remain gapless at $k = 0$, but the huge degeneracy is lifted. The gap is then much smaller than the external fields, and therefore the thermal excitations through the gap contribute to the thermodynamic properties at relatively low temperature. This is observed in the maximal entropy $S = \ln 2$ per unit cell being robust for not too large external field, as shown in Fig. 12. The high degeneracy revealed by finite entropy at low temperature suggests that the $\theta = \pi/2$ compass model may have potential applications in quantum computation [88]. In contrast, the entropy S of the Fermi liquid vanishes at zero temperature for $\theta \neq \pi/2$ according to the third law of thermodynamics.

In summary, we have shown that the polarization as a function of the electric field is strongly affected by the magnetic field. Similarly, the electric field has an effective impact upon the magnetization, which depends on the strength of the magnetic field. Strong variation of correlation functions and thermodynamic quantities are encountered by varying both electric and magnetic fields in the vicinity of a quantum critical point, where the magnetoelectric tensor demonstrates singularities at zero temperature. Remarkably, two characteristic temperature scales are uncovered. For $T < T_1 \approx 0.05$, the magnetization saturates in all three phases at large values, similar to the electric polarization P^y in the chiral phase, whereas in the other two phases P^y drops to small (but finite) values. Within the intermediate temperature range, $T_1 < T < T_2$, the thermal excitation admixes the features of the chiral state and the nonchiral state. As long as the thermal energy overcomes the bandwidth for $T > T_2$, the high temperature will wipe out the chiral features. This leads to a characteristic reentrant behavior of the electric polarization P^y in the canted Néel and the ferropolarized phases.

Note added in proof. We note, that knowing the mapping in Eq. (2.3), which is different for different materials, one can directly use all our relations which feature the dependence on the field E . Interestingly the control of DM interaction may also be extended to oscillating electric fields which may allow

for an externally driven rotation of spins [89,90]. Moreover, our work sheds light on the topological phase transitions in strongly correlated systems through the mapping of the complex spin Hamiltonian into the framework of independent electrons. Thereby the topological phase transition between the canted Néel or the polarized phase and the chiral phase, respectively, acquires a different and perhaps simpler interpretation than in the original spin model.

ACKNOWLEDGMENTS

W.L.Y. acknowledges the helpful discussion with R. Tang. This work is supported by the National Natural Science Foundation of China (NSFC) under Grants No. 11474211 and No. 11347008, as well as the Natural Science Foundation of Jiangsu Province of China under Grant No. BK20141190. A.M.O. acknowledges support from the Polish National Science Center (NCN) under Project No. 2012/04/A/ST3/00331.

-
- [1] M. Fiebig, *J. Phys. D* **38**, R123 (2005).
- [2] T. Kimura, T. Goto, H. Shintani, K. Ishizaka, T. Arima, and Y. Tokura, *Nature (London)* **426**, 55 (2003).
- [3] S.-W. Cheong and M. Mostovoy, *Nat. Mater.* **6**, 13 (2007).
- [4] Y. Kitagawa, Y. Hiraoka, T. Honda, T. Ishikura, H. Nakamura, and T. Kimura, *Nat. Mater.* **9**, 797 (2010).
- [5] S. Lee, M. T. Fernandez-Diaz, H. Kimura, Y. Noda, D. T. Adroja, S. Lee, J. Park, V. Kiryukhin, S.-W. Cheong, M. Mostovoy, and J.-G. Park, *Phys. Rev. B* **88**, 060103(R) (2013).
- [6] Y. J. Choi, H. T. Yi, S. Lee, Q. Huang, V. Kiryukhin, and S.-W. Cheong, *Phys. Rev. Lett.* **100**, 047601 (2008).
- [7] Y. Tokunaga, S. Iguchi, T. Arima, and Y. Tokura, *Phys. Rev. Lett.* **101**, 097205 (2008).
- [8] H. Katsura, N. Nagaosa, and A. V. Balatsky, *Phys. Rev. Lett.* **95**, 057205 (2005); M. Mostovoy, *ibid.* **96**, 067601 (2006).
- [9] M. Date, J. Kanamori, and M. Tachiki, *J. Phys. Soc. Jpn.* **16**, 2589 (1961).
- [10] V. Yu. Pomjakushin, M. Kenzelmann, A. Dönni, A. B. Harris, T. Nakajima, S. Mitsuda, M. Tachibana, L. Keller, J. Mesot, H. Kitazawa, and E. Takayama-Muromach, *New J. Phys.* **11**, 043019 (2009).
- [11] T. Kimura, *Annu. Rev. Mater. Res.* **37**, 387 (2007).
- [12] M. Soda, T. Ishikura, H. Nakamura, Y. Wakabayashi, and T. Kimura, *Phys. Rev. Lett.* **106**, 087201 (2011).
- [13] Y. Tokura and S. Seki, *Adv. Mater.* **22**, 1554 (2010).
- [14] I. A. Sergienko and E. Dagotto, *Phys. Rev. B* **73**, 094434 (2006).
- [15] S. Seki, X. Z. Yu, S. Ishiwata, and Y. Tokura, *Science* **336**, 198 (2012).
- [16] T. Adams, A. Chacon, M. Wagner, A. Bauer, G. Brandl, B. Pedersen, H. Berger, P. Lemmens, and C. Pfleiderer, *Phys. Rev. Lett.* **108**, 237204 (2012).
- [17] J. H. Yang, Z. L. Li, X. Z. Lu, M.-H. Whangbo, S.-H. Wei, X. G. Gong, and H. J. Xiang, *Phys. Rev. Lett.* **109**, 107203 (2012).
- [18] M. Matsuda, R. S. Fishman, T. Hong, C. H. Lee, T. Ushiyama, Y. Yanagisawa, Y. Tomioka, and T. Ito, *Phys. Rev. Lett.* **109**, 067205 (2012).
- [19] K. Yu. Povarov, A. I. Smirnov, O. A. Starykh, S. V. Petrov, and A. Ya. Shapiro, *Phys. Rev. Lett.* **107**, 037204 (2011).
- [20] H. Karimi and I. Affleck, *Phys. Rev. B* **84**, 174420 (2011).
- [21] W.-L. You and Y.-L. Dong, *Eur. Phys. J. D* **57**, 439 (2010); *Phys. Rev. B* **84**, 174426 (2011).
- [22] J. H. H. Perk, H. W. Capel, M. J. Zuilhof, and Th. J. Siskens, *Phys. A (Amsterdam, Neth.)* **81**, 319 (1975).
- [23] Z. Ming, Xu Hui, L. Xiao-Xian, and T. Pei-Qing, *Chin. Phys. B* **22**, 090313 (2013).
- [24] M. Brockmann, A. Klümper, and V. Ohanyan, *Phys. Rev. B* **87**, 054407 (2013).
- [25] S. Park, Y. J. Choi, C. L. Zhang, and S.-W. Cheong, *Phys. Rev. Lett.* **98**, 057601 (2007).
- [26] F. Schrettle, S. Krohns, P. Lunkenheimer, J. Hemberger, N. Büttgen, H.-A. Krug von Nidda, A. V. Prokofiev, and A. Loidl, *Phys. Rev. B* **77**, 144101 (2008).
- [27] S. Seki, T. Kurumaji, S. Ishiwata, H. Matsui, H. Murakawa, Y. Tokunaga, Y. Kaneko, T. Hasegawa, and Y. Tokura, *Phys. Rev. B* **82**, 064424 (2010).
- [28] Z. Nussinov and E. Fradkin, *Phys. Rev. B* **71**, 195120 (2005).
- [29] B. Douçot, M. V. Feigel'man, L. B. Ioffe, and A. S. Ioselevich, *Phys. Rev. B* **71**, 024505 (2005).
- [30] J. Dorier, F. Becca, and F. Mila, *Phys. Rev. B* **72**, 024448 (2005).
- [31] W. Brzezicki and A. M. Oleś, *Phys. Rev. B* **82**, 060401 (2010); **87**, 214421 (2013); *J. Phys. Conf. Ser.* **200**, 012017 (2010).
- [32] A. Kitaev, *Ann. Phys.* **321**, 2 (2006).
- [33] G. Baskaran, S. Mandal, and R. Shankar, *Phys. Rev. Lett.* **98**, 247201 (2007).
- [34] W. Brzezicki, J. Dziarmaga, and A. M. Oleś, *Phys. Rev. B* **75**, 134415 (2007); W. Brzezicki and A. M. Oleś, *Acta Phys. Polon. A* **115**, 162 (2009).
- [35] W.-L. You, P. Horsch, and A. M. Oleś, *Phys. Rev. B* **89**, 104425 (2014).
- [36] L. Cincio, J. Dziarmaga, and A. M. Oleś, *Phys. Rev. B* **82**, 104416 (2010).
- [37] W.-L. You and G.-S. Tian, *Phys. Rev. B* **78**, 184406 (2008); W.-L. You, *Eur. Phys. J. B* **85**, 83 (2012); G. H. Liu, W. Li, and W.-L. You, *ibid.* **85**, 168 (2012).
- [38] G.-H. Liu, W. Li, W.-L. You, G.-S. Tian, and G. Su, *Phys. Rev. B* **85**, 184422 (2012).
- [39] D. Xiao, W. Zhu, Y. Ran, N. Nagaosa, and S. Okamoto, *Nat. Commun.* **2**, 596 (2011).
- [40] J. Simon, W. S. Bakr, R. Ma, M. Eric Tai, P. M. Preiss, and M. Greiner, *Nature (London)* **472**, 307 (2011).
- [41] G. Sun, G. Jackeli, L. Santos, and T. Vekua, *Phys. Rev. B* **86**, 155159 (2012).
- [42] E. Barouch and B. M. McCoy, *Phys. Rev. A* **2**, 1075 (1970); **3**, 786 (1971).
- [43] A. Y. Kitaev, *Phys. Usp.* **44**, 131 (2001).
- [44] A. Altland and M. R. Zirnbauer, *Phys. Rev. B* **55**, 1142 (1997).
- [45] J. C. Budich and E. Ardonne, *Phys. Rev. B* **88**, 075419 (2013).
- [46] M. E. Zhitomirsky and A. Honecker, *J. Stat. Mech.* (2004) P07012.
- [47] Y. Niu, S. B. Chung, C.-H. Hsu, I. Mandal, S. Raghu, and S. Chakravarty, *Phys. Rev. B* **85**, 035110 (2012).
- [48] T. J. Osborne and M. A. Nielsen, *Phys. Rev. A* **66**, 032110 (2002).

- [49] J. Jeong, E. A. Goremychkin, T. Guidi, K. Nakajima, G. S. Jeon, S.-A. Kim, S. Furukawa, Y. B. Kim, S. Lee, V. Kiryukhin, S.-W. Cheong, and J.-G. Park, *Phys. Rev. Lett.* **108**, 077202 (2012).
- [50] G.-H. Liu, Wei Li, W.-L. You, G. Su, and G.-S. Tian, *Eur. Phys. J. B* **86**, 227 (2013).
- [51] G. Vidal, *Phys. Rev. Lett.* **98**, 070201 (2007).
- [52] L. Amico, R. Fazio, A. Osterloh, and V. Vedral, *Rev. Mod. Phys.* **80**, 517 (2008).
- [53] J. Eisert, M. Cramer, and M. B. Plenio, *Rev. Mod. Phys.* **82**, 277 (2010).
- [54] W.-L. You and W.-L. Lu, *Int. J. Mod. Phys. B* **25**, 231 (2011); W.-L. You, A. M. Oleś, and P. Horsch, *Phys. Rev. B* **86**, 094412 (2012).
- [55] A. M. Oleś, *J. Phys. Condens. Matter* **24**, 313201 (2012).
- [56] D. Gottesman and M. B. Hastings, *New J. Phys.* **12**, 025002 (2010).
- [57] P. Calabrese and J. Cardy, *J. Stat. Mech.* (2004) P06002.
- [58] T. Barthel, M. C. Chung, and U. Schollwöck, *Phys. Rev. A* **74**, 022329 (2006).
- [59] D. Gioev and I. Klich, *Phys. Rev. Lett.* **96**, 100503 (2006).
- [60] I. Klich and L. Levitov, *Phys. Rev. Lett.* **102**, 100502 (2009).
- [61] H. F. Song, C. Flindt, S. Rachel, I. Klich, and K. Le Hur, *Phys. Rev. B* **83**, 161408 (2011).
- [62] H. F. Song, S. Rachel, C. Flindt, I. Klich, N. Laflorencie, and K. Le Hur, *Phys. Rev. B* **85**, 035409 (2012).
- [63] Hui Li and F. D. M. Haldane, *Phys. Rev. Lett.* **101**, 010504 (2008).
- [64] B. Swingle and T. Senthil, *Phys. Rev. B* **86**, 045117 (2012).
- [65] J. Sirker, A. Herzog, A. M. Oleś, and P. Horsch, *Phys. Rev. Lett.* **101**, 157204 (2008).
- [66] F. Pollmann, E. Berg, A. M. Turner, and M. Oshikawa, *Phys. Rev. B* **85**, 075125 (2012).
- [67] F. Pollmann, A. M. Turner, E. Berg, and M. Oshikawa, *Phys. Rev. B* **81**, 064439 (2010).
- [68] F. Pollmann, S. Mukerjee, A. M. Turner, and J. E. Moore, *Phys. Rev. Lett.* **102**, 255701 (2009).
- [69] C. N. Yang and T. D. Lee, *Phys. Rev.* **87**, 404 (1952); T. D. Lee and C. N. Yang, *ibid.* **87**, 410 (1952).
- [70] B.-B. Wei and R.-B. Liu, *Phys. Rev. Lett.* **109**, 185701 (2012).
- [71] X. Liu, M. Zhong, H. Xu, and P. Tong, *J. Stat. Mech.* (2012) P01003.
- [72] K. A. Al-Hassanieh, C. D. Batista, G. Ortiz, and L. N. Bulaevskii, *Phys. Rev. Lett.* **103**, 216402 (2009).
- [73] N. Momozawa and Y. Yamaguchi, *J. Phys. Soc. Jpn.* **62**, 1292 (1993).
- [74] S. Ishiwata, Y. Taguchi, H. Murakawa, Y. Onose, and Y. Tokura, *Science* **319**, 1643 (2008).
- [75] L. Pauling, *J. Am. Chem. Soc.* **57**, 2680 (1935).
- [76] I. Affleck, *Phys. Rev. Lett.* **56**, 746 (1986).
- [77] H. W. J. Blöte, J. L. Cardy, and M. P. Nightingale, *Phys. Rev. Lett.* **56**, 742 (1986).
- [78] J. L. Cardy, *J. Phys. A* **17**, L385 (1984); **17**, L957 (1984); *Nucl. Phys. B* **240**, 514 (1984).
- [79] C. Trippé, A. Honecker, A. Klümper, and V. Ohanyan, *Phys. Rev. B* **81**, 054402 (2010).
- [80] B. Swingle and T. Senthil, *Phys. Rev. B* **87**, 045123 (2013).
- [81] T. T. Giamarchi, *Quantum Physics in One Dimension* (Clarendon, Oxford, 2004).
- [82] W.-L. You, G.-S. Tian, and H.-Q. Lin, *Phys. Rev. B* **75**, 195118 (2007).
- [83] K. Matsuhira, Z. Hiroi, T. Tayama, S. Tagaki, and T. Sakakibara, *J. Phys. Condens. Matter* **14**, L559 (2002).
- [84] A. W. Rost, R. S. Perry, J.-F. Mercure, A. P. Mackenzie, and S. A. Grigera, *Science* **325**, 1360 (2009).
- [85] T.-L. Ho and Qi Zhou, *Proc. Natl. Acad. Sci. USA* **106**, 6916 (2009).
- [86] J. Catani, G. Barontini, G. L'amporesi, F. Rabatti, G. Thalhammer, F. Minardi, S. Stringari, and M. Inguscio, *Phys. Rev. Lett.* **103**, 140401 (2009).
- [87] D. McKay and B. DeMarco, *Rep. Prog. Phys.* **74**, 054401 (2011).
- [88] L. del Rio, J. Åberg, R. Renner, O. Dahlsten, and V. Vedral, *Nature (London)* **474**, 61 (2011).
- [89] Wei Chen and M. Sgrist, *Phys. Rev. B* **89**, 024511 (2014).
- [90] Wei Chen, P. Horsch, and D. Manske, *Phys. Rev. B* **89**, 064427 (2014).